

INTERNAL STRUCTURE OF PROTOCLUSTER GALAXIES: ACCELERATED STRUCTURAL EVOLUTION IN OVERDENSE ENVIRONMENTS?¹

ANDREW W. ZIRM², SUNE TOFT², AND MASAYUKI TANAKA³

Draft version November 10, 2018

ABSTRACT

We present a high spatial-resolution *HST*/NICMOS imaging survey in the field of a known proto-cluster surrounding the powerful radio galaxy MRC1138-262 at $z = 2.16$. Previously, we have shown that this field exhibits a substantial surface overdensity of red $J - H$ galaxies. Here we focus on the stellar masses and galaxy effective radii in an effort to compare and contrast the properties of likely protocluster galaxies with their field counterparts and to look for correlations between galaxy structure and (projected) distance relative to the radio galaxy.

We find a hint that quiescent, cluster galaxies are on average less dense than quiescent field galaxies of similar stellar mass and redshift. In fact, we find only two (of nine) quiescent protocluster galaxies are of similar density to the majority of the massive, quiescent compact galaxies (SEEDs) found in several field surveys. Furthermore, there is some indication that the structural Sersic n parameter is higher ($n \sim 3 - 4$) on average for cluster galaxies compared to the field SEEDs ($n \sim 1 - 2$). This result may imply that the accelerated galaxy evolution expected (and observed) in overdense regions also extends to structural evolution presuming that massive galaxies began as dense (low n) SEEDs and have already evolved to be more in line with local galaxies of the same stellar mass.

Subject headings: galaxies: clusters: individual (MRC1138-262) – galaxies: evolution – galaxies: high-redshift – galaxies: structure

1. INTRODUCTION

The internal spatial and velocity distribution of stars is an indicator of the manner in which galaxies have formed, assembled and evolved. In the local universe, tidal streams, shells and kinematically distinct cores are examples of archeological clues to past merging and formation events (e.g., Peng et al. 2002b; Emsellem et al. 2007; van Dokkum 2005; Blanton & Moustakas 2009). Even coarse measures, such as the average stellar surface mass density within the effective radius (Σ_{50}), correlate with the star formation rate or the mean stellar age. Giant elliptical galaxies have high stellar mass per unit area (or volume) and show negligible current star formation while more diffuse stellar disks and dwarf irregulars are forming stars at sometimes prodigious rates per unit stellar mass (specific star-formation rate; sSFR). At higher redshift, analogous relations are already in place (e.g., Franx et al. 2008). While observationally it remains difficult to separate high-redshift galaxies into classical Hubble-types we can now photometrically determine redshifts, stellar masses and galaxy sizes for large numbers of galaxies at $z \sim 2$. Such studies (e.g., Zirm et al. 2007; Toft et al. 2007; van Dokkum et al. 2008; Toft et al. 2009; Williams et al. 2010; Mosleh et al. 2011) have found that quiescent galaxies are in general more dense than their star-forming counterparts.

The origin of this bi-modal distribution of galaxy properties is unclear. It is possible that the quiescent $z \sim 2$ galaxies are more compact because they formed when the universe was smaller and more dense and mergers were more gas-rich. It also seems plausible that the process which quenches star formation may be linked to a morphological change. Or perhaps the dominant formation processes differ for galaxies with different present-day stellar masses (Khochfar & Silk 2006, 2009, 2011; Dekel & Birnboim 2008; Dekel et al. 2009).

In general terms, dissipation should result in more compact stellar cores than dissipationless assembly (e.g., Ciotti, Lanzoni, & Volonteri 2007; Naab, Johansson, & Ostriker 2009; Oser et al. 2010). Dense stellar systems, once formed, tend to persist through successive (minor) mergers. The relatively recent discovery of quiescent, massive and compact galaxies at $z \sim 2$ (hereafter Semi-Evolved Elephantine Dense galaxies or “SEEDs”) implies that at least some galaxies have their origin in high-redshift ($z \gtrsim 4$), gas-rich mergers (Daddi et al. 2005; Zirm et al. 2007; Toft et al. 2007; van Dokkum et al. 2008; Cimatti et al. 2008). These mergers resulted in many stars being formed in a relatively small volume. By $z \sim 2$ these systems have low star-formation rates and relatively high stellar masses in addition to their small sizes ($r_e \lesssim 1$ kpc). The SEEDs therefore have extreme internal stellar mass densities. They do not fall on the size-mass relation defined by local galaxies. Their evolution from $z \sim 2$ to $z = 0$ is therefore a puzzle.

The most massive galaxies in the present-day universe are located at the centers of rich clusters. These galaxy overdensities were statistically the first to separate from the Hubble flow and collapse and are therefore believed to follow an accelerated timeline for the process of galaxy formation. There is some observational evidence that

¹ Based on observations with the NASA/ESA Hubble Space Telescope, obtained at the Space Telescope Science Institute, which is operated by the Association of Universities for Research in Astronomy, Inc., under NASA contract NAS 5-26555

² Dark Cosmology Centre, Niels Bohr Institute, University of Copenhagen, Juliane Maries Vej 30, DK-2100 Copenhagen, Denmark; azirm@dark-cosmology.dk; sune@dark-cosmology.dk

³ Institute for the Physics and Mathematics of the Universe, The University of Tokyo, 5-1-5 Kashiwanoha, Kashiwa, Chiba 277-8583, Japan; masayuki.tanaka@ipmu.jp

galaxies in the progenitors of clusters, protoclusters, do have significantly older stars and higher masses than galaxies in the field at similar redshifts (Steidel et al. 2005; Tanaka et al. 2010). Might cluster galaxies, having formed earlier, be even more dense than field SEEDS? Or, alternatively, the ‘fast-forward’ evolution of cluster galaxies may lead to lower density galaxies in protoclusters compared to their field counterparts. It is interesting, then, to look for dense SEED galaxies in protoclusters at redshift $z \sim 2$.

We have undertaken a NICMOS imaging program to study the red galaxy population in a protocluster at $z = 2.16$. Broad and narrow-band imaging, both in the optical and near-infrared, of the field surrounding the powerful radio galaxy MRC 1138-262 ($z = 2.16$) have identified more than 100 candidate companion galaxies. There are surface-overdensities of both line-emitting candidates (Lyman- α and H α), X-ray point sources, sub-mm selected galaxies and red optical-near-infrared galaxies (Pentericci et al. 2002; Kurk 2003; Kurk et al. 2004b; Stevens et al. 2003; Croft et al. 2005). Fifteen of the Ly α and 9 of the H α emitters have been spectroscopically confirmed to lie at the same redshift as the radio galaxy (Kurk et al. 2004a). By obtaining deep images through the NICMOS J_{110} and H_{160} filters, which effectively span the 4000Å-break at $z = 2.16$, we have identified a large surface overdensity of red galaxies consistent with a forming red sequence (Zirm et al. 2008). In this paper we present a more detailed analysis of the masses and morphologies of galaxies in this field. The article is organized as follows: in Section §?? we describe the data and their reductions, in Section §?? we present the photometric redshifts, stellar population models and morphological fits, in Section §?? we present the internal stellar mass densities and other derived properties and finally in §?? we discuss these results in the context of galaxy evolution models. We use a $(\Omega_{\Lambda}, \Omega_M) = (0.7, 0.3)$, $H_0 = 73$ km s $^{-1}$ Mpc $^{-1}$ cosmology throughout. At $z = 2.16$ one arcsecond is equivalent to 8.4 kpc. All magnitudes are referenced to the AB system (Oke 1974) unless otherwise noted.

2. OBSERVATIONS AND DATA REDUCTIONS

2.1. NICMOS Imaging

The NICMOS instrument on-board *HST* is capable of deep near-infrared imaging over a relatively small field-of-view ($51'' \times 51''$). In the case of MRC 1138-262, we know that galaxies are overdense on the scale of a few arcminutes (Kurk et al. 2004b; Croft et al. 2005) and are thus well-suited for observations with NICMOS camera 3 on *HST*. We used 30 *HST* orbits to image seven overlapping pointings in both filters and one additional pointing in H_{160} alone. These observations reach an AB limiting magnitude ($m_{10\sigma}$; 10σ , $0''.5$ diameter circular aperture) of $m_{10\sigma} = 24.9$ mag in J_{110} and $m_{10\sigma} = 25.1$ mag in H_{160} . The same field was imaged in the g_{475} ($m_{10\sigma} = 27.5$ mag) and I_{814} ($m_{10\sigma} = 26.8$ mag) filters using the Wide-Field Channel of the Advanced Camera for Surveys on *HST* as part of a Guaranteed Time program (# 10327; Miley et al. 2006).

The NICMOS images were reduced using the on-the-fly reductions from the *HST* archive, the IRAF task *pedsky* and the *dither/drizzle* package to combine the images in

a mosaic. The dither offsets were calculated using image cross-correlation and were refined iteratively. Alignment of the pointings relative to each other was accomplished using a rebinned version of the ACS I_{814} image as a reference. The final mosaic has a pixel scale of $0''.1$. Galaxies were selected using the H_{160} -band image for detection within SExtractor (Bertin & Arnouts 1996). We used a 2.2σ detection threshold with a minimum connected area of 10 pixels. We also corrected the NICMOS data for the count-rate dependent non-linearity (de Jong 2006). Total galaxy magnitudes were estimated by using the MAG_AUTO values from SExtractor. We show the outline of the NICMOS mosaic in Figure 1 along with the positions of the radio galaxy (yellow star) and star-forming (blue circles) and quiescent (red circles) protocluster galaxies.

The $J_{110} - H_{160}$ colors were determined by running SExtractor (Bertin & Arnouts 1996) in two-image mode using the H_{160} image for object detection and isophotal apertures. The J_{110} image was PSF-matched to the H_{160} band. We also incorporated the two ACS bands (Miley et al. 2006), the Spitzer IRAC bands, U_n (Zirm et al. 2008) and V bands from Keck/LRIS, z and R from VLT/FORS2 (Kurk et al. 2004b,a), H band from NTT/SOFI and J and K_s from Subaru/MOIRCS (Kodama et al. 2007). The assembly of the merged multi-band catalog is detailed in Tanaka et al. 2010.

2.2. FIREWORKS Survey Data and Literature Sample

The FIREWORKS data are described in detail in Wuyts et al. (2008). In brief, the survey is K_S -band selected to 5σ depth of 24.3 (AB) over an area of 113Mpc^2 . In addition to the deep K_S band data there is high-quality imaging in each of the U, B, V, I, i, z, J, H , the four *Spitzer*/IRAC bands and the $24\mu\text{m}$ *Spitzer*/MIPS band. The combined multi-band catalog has been used to measure precise photometric redshifts, galaxy sizes (Toft et al. 2009) and to model the spectral energy distributions to derive stellar masses, ages and star-formation rates (Damen et al. 2009). We have made three cuts to the FIREWORKS sample to ensure that we are making appropriate field-to-cluster comparisons. First, since we are comparing galaxy sizes (densities) we require that the galaxies are bright enough to have a reliable size measurement in these ground-based data. Based on the comparison of size measurements from VLT/ISAAC and *HST*/NICMOS for the same galaxies, Toft et al. (2009) found that at $K \sim 21.5 - 22.0$ the scatter between these two size determinations increases significantly. We therefore select only $K < 21.5$ galaxies from FIREWORKS. Next, we have made a photometric redshift cut $1.9 < z < 2.6$ to select galaxies within the field at roughly the same epoch as the protocluster galaxies. Finally, we select the quiescent field population on the basis of the specific star-formation rate ($\log(\text{sSFR}) < -11 \text{ yr}^{-1}$). We note that after these cuts, the stellar mass distribution remains similar to our protocluster galaxy sample.

For further comparison to our protocluster field data, we have compiled a sample of $z \sim 2$ quiescent galaxies published in the literature. We used four references for this sample: Cassata et al. (2010), van Dokkum et al. (2008), Mancini et al. (2010) and Saracco, Longhetti, & Andreon (2009). Saracco, Longhetti, & Andreon (2009) used *HST*/NICMOS Camera 3 as we have, Mancini

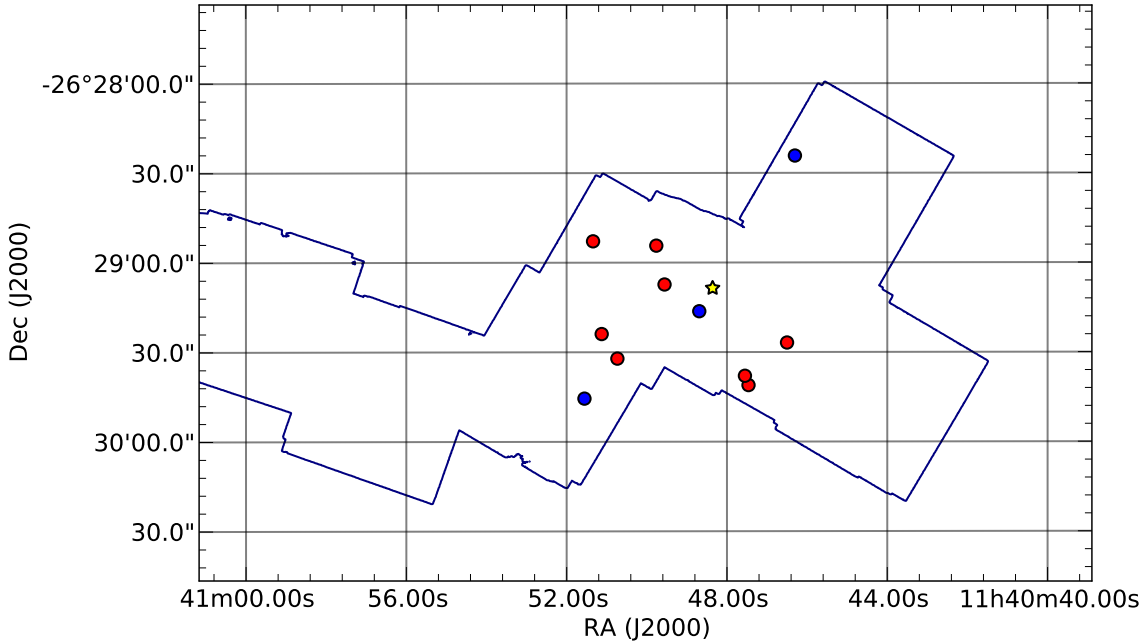


Figure 1. Outline of the NICMOS mosaic. The red and blue points mark the locations of the quiescent and star-forming cluster galaxies respectively. The yellow star is the radio galaxy MRC1138-262.

et al. (2010) used *HST*/ACS imaging, van Dokkum et al. (2008) studied *HST*/NICMOS Camera 2 imaging while Cassata et al. (2010) use imaging from the WFC3/IR channel on *HST*.

We have attempted to translate these published stellar mass estimates to the same IMF (Salpeter) and to the same stellar population synthesis model set (Maraston 2005). We have used the analyses of Salimbeni et al. (2009; see their Fig. 1) to derive mean corrections between model sets. The adopted IMF also affects the derived star-formation rates. The offsets in this quantity are similar in magnitude to the systematic shift in derived stellar mass (e.g., Erb et al. 2006; Nordon et al. 2010), so the specific star formation rate (i.e., the ratio of star-formation rate to stellar mass) should be effectively unchanged.

3. ANALYSIS

Here we combine the multiband photometric catalog and the NICMOS high spatial-resolution imaging to derive physical parameters for individual galaxies. We pare down the total NICMOS galaxy sample to those which have a high quality-of-fit for the photometric redshift (using EAZY, Brammer, van Dokkum, & Coppi (2008)), the spectral energy distribution (using FAST, Kriek et al. (2009)) and 2D surface-brightness profile fit (using GALFIT, Peng et al. (2002a)). This reduces the galaxy sample from the H_{160} -band detected total of 711. We further restrict our attention to those galaxies which most likely lie within the known protocluster (see Section §3.4).

3.1. Photometric Redshifts

The thirteen filter photometric catalog (Tanaka et al. 2010) was used to determine galaxy photometric redshifts. We used the public code, EAZY, to fit a set of model templates to each galaxy’s photometric data (Brammer, van Dokkum, & Coppi 2008). We required

that each galaxy have at least 5 colors measured for the photometric redshift fit. The set of SED templates we used included both galaxy spectral energy distributions and a narrow emission line spectrum. EAZY uses all linear combinations of the input templates to find the best photometric redshift fit. For each fit, EAZY produces the full redshift probability distribution (see Figs. 2 - 4). We are most interested in the galaxies detected in the relatively small ($\sim 5\text{''}$), but deep, NICMOS H_{160} -band area. Therefore, we have only included sources detected in the H_{160} NICMOS images. For the target redshift of $z = 2.2$, the primary strong spectral feature covered by the photometric data is the 4000\AA break. We note that even with 13 bands of imaging, photo-zs are not sufficiently precise to determine whether a galaxy is inside the cluster or not. There are 12 spectroscopically confirmed (emission line) protocluster members within the NICMOS mosaic. Of these, four $H\alpha$ and one $\text{Ly}\alpha$ emitters have well-determined photometric redshifts (the remaining members are generally too faint to have detections in enough bands). Four of the five photo-zs are around $z \sim 2.1$, ranging from 1.8 to 2.1. There is one clear outlier, the $H\alpha$ emitter with $z_{\text{phot}} = 0.33$.

3.2. Stellar Population Modeling

Using the calculated best-fit photometric redshifts, we used FAST (Kriek et al. 2009) to fit stellar population model templates to the rest-frame photometry. These templates consist of a grid of models drawn from the Maraston (2005) set. We chose to use the Salpeter IMF, exponentially declining star-formation histories with τ varying between 10^7 and 10^{10} years and A_V between 0 and 3 magnitudes. FAST calculates the best-fitting model template among the grid and thereby derives a luminosity-weighted mean stellar age, stellar mass, star-formation rate and extinction for each galaxy. FAST also outputs the 1σ error estimates for each of these fit pa-

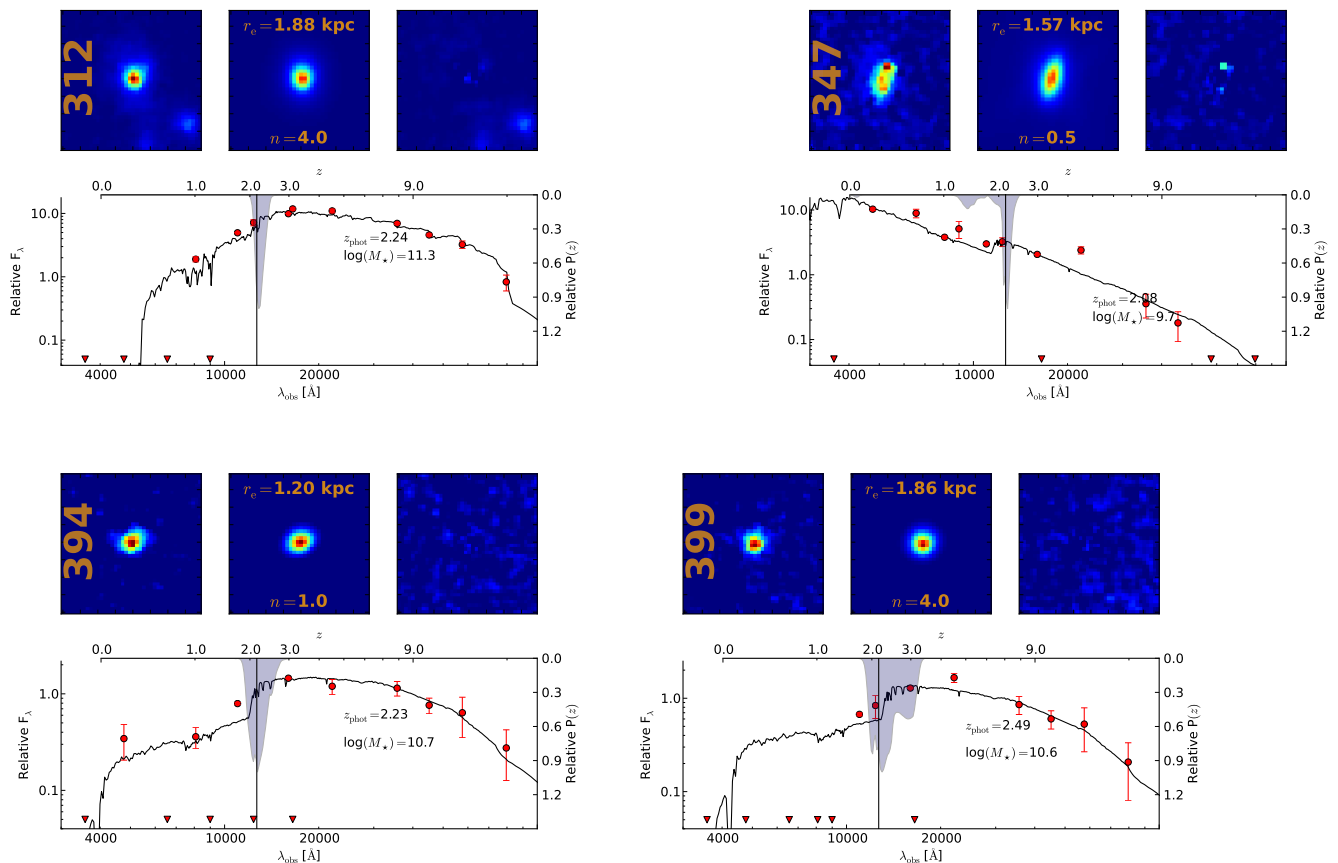


Figure 2. Upper panels, left to right: Galaxy image, GALFIT best-fit model and image residuals after subtraction of the model. Lower panel: Photometry and best-fit SED model from FAST (red circles and solid black line Kriek et al. 2009). The shaded regions represent the photometric redshift probability distribution (upper scale) centered at rest-frame 4000Å.

rameters. We show the derived masses and their errors for the protocluster galaxies in Table 1. We note that the star-formation rates from SED fitting are equivalent to a dust-corrected rest-frame UV SFR and that none of our quiescent protocluster galaxies have significant detections in the MIPS 24 μm image (20693, PI: Stanford). Since we are only concerned with differentiating the quiescent and star-forming galaxies, our results are sensitive only to catastrophic errors in these SFR determinations.

3.3. NICMOS Galaxy Sizes and Morphologies

NICMOS camera 3 provides good angular resolution over its field-of-view (PSF FWHM $\approx 0''.27$). To exploit this resolution we have used the GALFIT code (Peng et al. 2002a) to fit analytic Sérsic surface-brightness profiles (Sérsic 1968) to all the $H_{160} \leq 26.5$ sources in our H_{160} -band mosaic. We have used our own error map as input to GALFIT for properly weighting the image pixels and have masked all neighboring objects. A model point-spread function was created for each of these galaxies individually by generating a TinyTim simulated PSF (Krist 1993) at the galaxies’ positions in each exposure and then drizzling these PSFs together in exactly the same fashion as for the data themselves (see Zirm et al. 2007). We then executed several different runs of GALFIT. We ran fits holding the Sérsic index constant at $n = 1$ and 4, using a single model PSF for all galaxies,

using a stellar PSF instead of the model(s) and holding the sky value fixed at zero. For all fits we restricted the Sérsic index, n , to be between 0.5 and 5. The range of output fit values for all these different runs gives us an idea of the variance of the derived parameters due to model assumptions. We choose the best fit from these runs by applying the F-test to the resultant χ^2_ν values.

The primary source of systematic offsets in galaxy profile and size fitting is the estimation of the local sky value. If the sky is underestimated the galaxy size can be overestimated, particularly for small faint galaxies. Therefore, we compare our fits where the sky level is a free parameter with those where we explicitly fix the sky to zero. Many of the “zero-sky” fits fail to converge, for those that do converge and have comparable chi-squared values to the corresponding free fits, we can compare the output r_e determinations. It does not appear to be the case that equally good fits are obtained with and without fitting the sky. In those five cases where an F-test shows the zero-sky fit to be better, the sizes agree within the errors. Furthermore, none of these where the zero-sky result is comparably good are for any of our protocluster galaxies. We note that the GALFIT sky values while non-zero are consistently several orders-of-magnitude smaller than the values corresponding to galaxy pixels. This sensitivity of the fit parameters to even slight variations in the sky highlights the importance of fitting the local sky

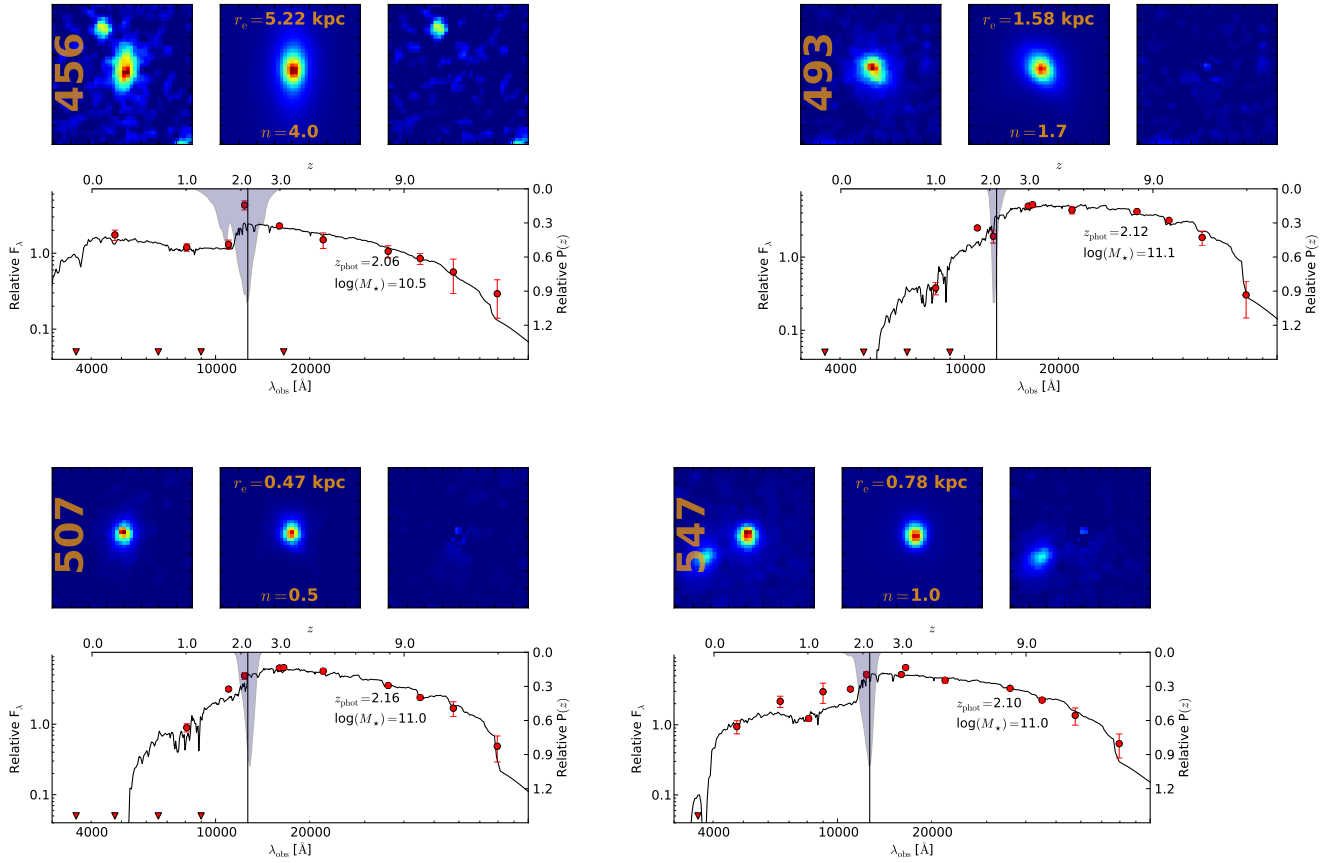


Figure 3. Fig. 1 cont.

along with the galaxy parameters (even in sky-subtracted data).

We also note that additional scatter to the derived r_e values introduced by using a stellar rather than model PSF is about 10 – 20% and therefore comparable to the scatter on the single-fit measurements themselves.

3.4. Sample Selections

We use the surface-brightness profile and stellar population fits along with the photometric redshifts to define three sub-samples of the NICMOS-detected galaxies. We detail these in order of increasing restriction. The initial sample is defined by a single H_{160} -band limit of 26.5 (AB) and consists of 711 galaxies.

3.4.1. GALFIT Sample

We ran GALFIT on the full H_{160} -limited galaxy sample. Using the distribution of GALFIT χ^2_ν values for the fits we identify galaxies with good quality-of-fit ($\chi^2_\nu < 2$; 577 of the input 711). We then calculate the circularized r_e ($= \sqrt{ab}$) for these well-fit galaxies. We use this GALFIT sample in our analysis of the dependence of the Sersic index, n , on radial position within the cluster (see left panel of Fig. 7). We note that we have re-normalized the input sigma (error) maps such that the best fits have $\chi^2_\nu \sim 1$.

3.4.2. Stellar Populations Sample

To select galaxies with good constraints on both the stellar mass and star-formation rate we have selected another sub-sample for the initial 711 galaxies. For targets with both good photo- z fits and narrow redshift probability distributions (ODDS > 0.90 , meaning 90% of the probability distribution is contained within the $\Delta z = 0.2$ around the peak value) the sample comprises 190 galaxies out of the 711. The photometry for these targets were fit using FAST. From this set we have identified 112 with reliably derived parameters ($\chi^2_\nu < 3.0$) based on the SED fits (for example, see Figs. 2-4).

3.4.3. Probable Protocluster Galaxies

Finally, we have identified a sample of candidate protocluster members using photometric redshifts. In lieu of spectroscopic redshifts, which are difficult to obtain for $z \sim 2$ red, quiescent galaxies, this selection should reject most of the interlopers. We consider only galaxies with a robust photometric redshift (as above) that have probability $P(z) > 20\%$ at the protocluster redshift ($z = 2.156$). We further require that these galaxies also are members of the ‘‘Stellar Populations’’ sample. These selections result in a sample of 11 galaxies, nine of which are quiescent ($\log_{10} \text{sSFR} < -11 \text{ yr}^{-1}$). We show the galaxy cutouts, the best-fit Sersic model, the model subtraction residuals, the broad-band SED fit and photometric redshift probability distribution for these galaxies in Figures 2-4.

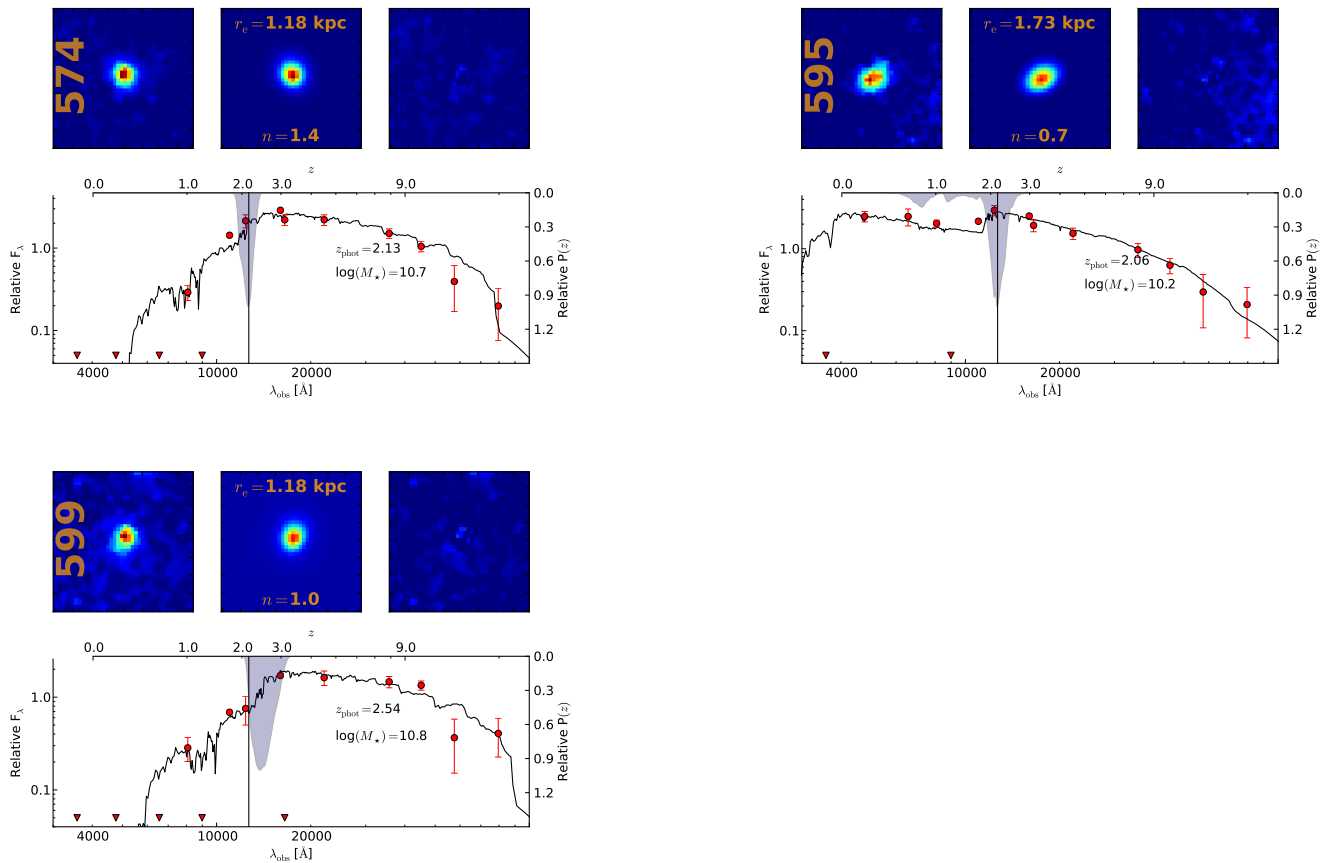


Figure 4. Fig. 1 cont.

3.5. Stellar Mass Density

The surface (volume) mass density in individual galaxies is a fundamental property which seems to correlate directly with the absence of star formation (e.g., Kauffmann et al. 2003; Franx et al. 2008). To measure this quantity requires accurate total mass estimates based on either stellar velocity dispersion or, much more commonly, the stellar mass from SED fits to the broad-band photometry. Along with the resolved surface-brightness profile to determine the galaxy size we can calculate the mass density. We must make the assumption that light traces mass and that there are no strong gradients in the stellar mass-to-light ratio, i.e., we measure M/L for the integrated galaxy light and assume that value applies to the resolved profile in a single broad-band image.

For our galaxies, we calculate the average surface mass density (Σ_{50} in $M_\odot \text{ kpc}^{-2}$) within the (circularized) effective radius (r_e) as follows:

$$\Sigma_{50} = \frac{M_\star/2}{\pi r_e^2} \quad (1)$$

We present our measurements in Table 1.

4. RESULTS

4.1. Distribution of Internal Surface Mass Densities

We have used the combination of photometric redshifts, stellar population modeling and surface-brightness

profile fits to calculate internal surface mass densities for our protocluster sample. We have also added data from the literature and from FIREWORKS to construct a well-populated density versus stellar mass diagram in Figure 5. If the published data had a measured star-formation rate in addition to the stellar mass we have restricted the points plotted to those with low sSFRs (quiescent; $\log_{10} \text{ sSFR} < -11 \text{ yr}^{-1}$). In cases where the star-formation rate was not quoted explicitly, we only plot those galaxies which are described as “quiescent” by the authors. This distribution for both our protocluster candidates (yellow circles and squares for quiescent and star-forming) and the field sources from the literature (black squares) and FIREWORKS (blue squares) is shown in Figure 5. For the comparison field sample we have restricted to FIREWORKS galaxies brighter than $K = 21.5$ and with photo- z between 1.9 and 2.6. We have made the same redshift cut for the literature sample. This redshift range approximately corresponds to a 1 Gyr epoch centered on the protocluster redshift.

The mean density of the protocluster sample ($\log < \Sigma_{50} > = 9.9$) is 0.5 dex lower than that for the field sample. For the stellar mass range of our protocluster sample, $10^{10.5} M_\odot < M_\star < 10^{11.4} M_\odot$, where the mass distributions are similar, we can calculate the distribution of the surface mass densities irrespective of total stellar mass. We have also used the KS test to calculate the probability that the (quiescent) protocluster and

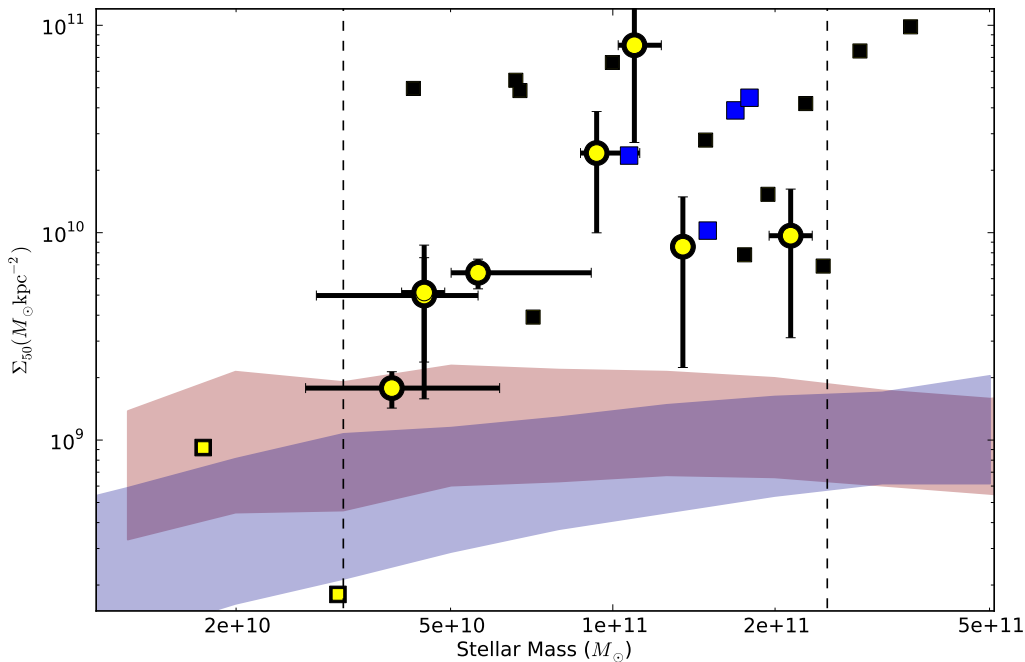


Figure 5. Surface stellar mass density (Σ) vs. total stellar mass for individual galaxies. The blue and black squares are from the FIREWORKS survey (Toft et al. 2009) and other literature (van Dokkum et al. 2008; Cassata et al. 2010; Mancini et al. 2010; Saracco, Longhetti, & Andreon 2009) respectively. The large blue squares are the $K > 21.5$ FIREWORKS galaxies included in the KS test. The yellow circles with error bars are the 8 likely quiescent protocluster members. The two yellow squares are the star-forming protocluster galaxies (the third falls at $5 \times 10^9 M_\odot$). The shaded regions are the local relations for early-type (light red) and late-type galaxies (light blue). Note that most of the protocluster members have lower densities than their field counterparts.

field densities are drawn from the same parent distribution. A fiducial value of $P_{KS} < 5\%$ may be considered sufficient to reject the null hypothesis that they are from the same parent. In this case $P_{KS} \sim 5\%$ and is therefore a relatively strong constraint. We have perturbed our measured densities and re-calculated P_{KS} for 10000 trials. We show the distribution of P_{KS} in Figure 6. For the black (yellow) histogram 30% (60%) of the realizations fall below $P_{KS} = 5\%$. Both histograms have tails to higher probabilities.

4.2. Radial Dependencies

In order to assess possible radial gradients in the galaxy properties within the cluster, with respect to the radio galaxy, we have constructed the histograms shown in Figure 7. For each of these four physical galaxy parameters: Sérsic n value, surface mass density (Σ), stellar mass (M_*) and specific SFR, we have made a single cut in the galaxy sample and plotted two radial histograms for above (orange) and below (blue) the chosen cut value. The left panel of Fig. 7 shows the histograms for the full galaxy sample appropriate to each parameter, i.e., the GALFIT sample for the Sérsic n value. For the rest, the galaxies must also be in the stellar population sample. The right panel shows the histograms for our protocluster galaxy sample (both quiescent and star-forming). We have presented these two analyses because while the presence of field galaxies in the larger samples will dilute any result, the statistics are poor for the quiescent protocluster galaxy sample. Furthermore, this field exhibits a factor of six surface overdensity of red galaxies (Zirm

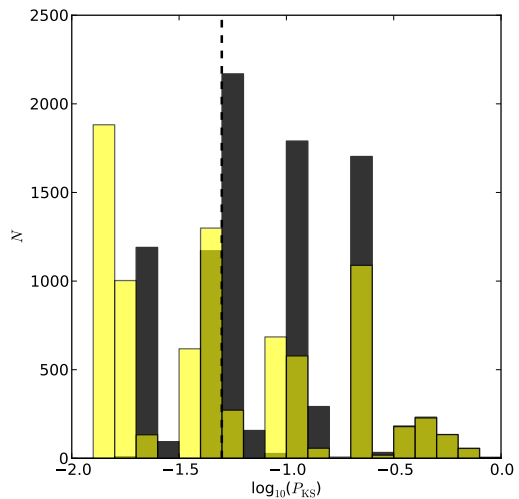


Figure 6. The KS probability distributions for the protocluster versus field galaxy comparison. The black histogram are derived from 10000 runs with the protocluster densities perturbed at random within the Gaussian errors. The yellow histogram is the same but excluding the most dense protocluster galaxy. The vertical dashed line marks $P_{KS} = 0.05$. About 55% of the realizations fall below the 5% probability.

et al. 2008), so the large sample may not strongly dilute trends.

For each pair of histograms we have run the two-sample KS test to determine whether the distributions are consistent with one another. However, for the full sample

(left) the Sersic n distributions are more dissimilar than for the other parameters with a low $P_{KS} = 5\%$. This low probability seems to be the result of a relatively flat distribution of the $n < 2.5$ galaxies with radius contrasting with the structure in the radial distribution of the higher n galaxies. This hint may imply a scenario in which the galaxies are deeper within the gravitational potential. We discuss this point further below. In the future, with spectroscopic redshifts for red galaxies, it will be possible to repeat this test with better interloper rejection to see if the discrepancy between histograms is significant for bona fide protocluster galaxies.

5. DISCUSSION

We have presented the combined analysis of 13 band photometry and high spatial-resolution NIR imaging in the field of a known galaxy protocluster at $z = 2.16$. In cases like this where there is a known, confirmed overdensity and strong statistical evidence for a dominant contribution from protocluster members we can make progress despite the lack of spectroscopic redshifts. We have identified a robust sample of likely protocluster galaxies. Our conclusions are tentative and tempered by the following caveats. We do not have spectroscopic redshifts for the quiescent cluster galaxies. While we have done our best to isolate the most probable cluster members, they may still be field galaxies. The cluster sample is also relatively small and the results are therefore more suggestive rather than statistically robust. Finally, due to the limited areal coverage of the protocluster (see Fig. 1), the very massive galaxies may be underrepresented in the cluster sample. These may also be more dense.

Possible stellar population model offsets have been minimized by converting the literature points to the same models and IMF we used to fit the cluster galaxies.

5.1. Evolution of Galaxy Structure and Stellar Mass Surface Density

From the initial discovery of SEEDs, in general field surveys, the primary question has been what evolutionary processes affect the SEEDs between $z \sim 2 - 3$ and $z = 0$ that bring them in line with the local mass-size relation. If the dominant process is galaxy merging, then we might expect that most of the full galaxy mergers, as opposed to tidal interactions and harassment, may have already happened. While if the primary determinant of galaxy density is the formation redshift, the young Universe being denser, we might expect that cluster galaxies will be denser than their field counterparts having formed earlier.

In our data we see some indication for a difference between the profile shapes and density distributions for protocluster versus field galaxies (Fig. 5). For our sample of likely quiescent protocluster galaxies their stellar densities are lower and perhaps even the Sersic index is higher than for similarly selected field galaxies. From other studies it appears that the majority of field SEEDs have higher axial ratios (flattened) with $n \sim 2$ (van der Wel et al. 2011).

5.2. Cosmic Merger Clocks

Several previous studies have shown evidence that protocluster galaxies tend to be more massive and contain

older stars than their field counterparts at the same redshift (e.g., Steidel et al. 2005; Tanaka et al. 2010). This advanced evolution in the cluster environment may also extend to the internal structure and dynamics of the galaxies. At lower redshift, we observe a morphology-density relation, and we may be seeing the beginnings of that relation in the MRC 1138 protocluster. Furthermore, the lower densities of the protocluster galaxies suggests that the necessary merging has also taken place at a quicker pace than in the field. If we assume then that all galaxies begin as dense SEEDs at high redshift, we can use the observed densities as a measure of the “merger age” of the remnants. A similar idea was put forth by Hopkins and Hernquist (2010) to derive the global star-formation history by using the mass profiles of galaxies. They propose that the dense cores of galaxies form early in starbursts and the outer parts form in a more quiescent mode, perhaps in disks. Based on the results from this paper we suggest that the resolved mass profiles can be used further to constrain the redshift of formation and the subsequent merger history. The ratio of high-density stellar mass to low-density stellar mass may tell us something about the merger age of a galaxy while the absolute density of the highest density stellar components may tell us about the formation redshift. Studies at low-redshift have already found some correlation between galaxy density and the mean stellar age (e.g., van der Wel et al. 2009). With more precise stellar ages for $z \sim 2$ galaxies now becoming available we can extend this analysis to high-redshift when the fractional age differences between galaxies are larger.

A. Zirm and S. Toft gratefully acknowledge support from the Lundbeck Foundation. The authors thank the anonymous referee for their helpful comments. This work is supported by World Premier International Research Center Initiative (WPI Initiative), MEXT, Japan and also in part by Grant-In-Aid for Young Scientists No. 23740144.

REFERENCES

- Bertin, E. & Arnouts, S. 1996, *A&AS*, 117, 393
 Blanton, M. R. & Moustakas, J. 2009, *ARA&A*, 47, 159
 Brammer, G. B., van Dokkum, P. G., & Coppi, P. 2008, *ApJ*, 686, 1503
 Cassata, P., et al. 2010, 714, 79
 Cimatti, A., et al. 2008, *A&A*, 482, 21
 Ciotti, L., Lanzoni, B., & Volonteri, M. 2007, *ApJ*, 658, 65
 Croft, S., Kurk, J., van Breugel, W., Stanford, S. A., de Vries, W., Pentericci, L., & Röttgering, H. 2005, *AJ*, 130, 867
 Daddi, E., et al. 2005, *ApJ*, 626, 680
 Damen, M., Förster Schreiber, N. M., Franx, M., Labbé, I., Toft, S., van Dokkum, P. G., & Wuyts, S. 2009, *ApJ*, 705, 617–623
 de Jong, R. 2006. Correcting the nicmos count-rate dependent non-linearity. Technical report, STScI
 Dekel, A. & Birnboim, Y. 2008, *MNRAS*, 383, 119
 Dekel, A., et al. 2009, *Nature*, 457, 451
 Emsellem, E., et al. 2007, *MNRAS*, 379, 401
 Erb, D. K., Steidel, C. C., Shapley, A. E., Pettini, M., Reddy, N. A., & Adelberger, K. L. 2006, *ApJ*, 647, 128
 Franx, M., van Dokkum, P. G., Schreiber, N. M. F., Wuyts, S., Labbé, I., & Toft, S. 2008, *ApJ*, 688, 770
 Hopkins, P. F. & Hernquist, L. 2010, *MNRAS*, 402, 985
 Kauffmann, G., et al. 2003, *MNRAS*, 341, 54–69
 Khochfar, S. & Silk, J. 2006, *ApJ*, 648, 21
 Khochfar, S. & Silk, J. 2009, *ApJ*, 700, 21

- Khochfar, S. & Silk, J. 2011, MNRAS, 410, L42
- Kodama, T., Tanaka, I., Kajisawa, M., Kurk, J., Venemans, B., De Breuck, C., Vernet, J., & Lidman, C. 2007, MNRAS, 377, 1717
- Kriek, M., van Dokkum, P. G., Labbé, I., Franx, M., Illingworth, G. D., Marchesini, D., & Quadri, R. F. 2009, ApJ, 700, 221
- Krist, J. 1993, in ASP Conf. Ser. 52: Astronomical Data Analysis Software and Systems II 536
- Kurk, J. D. 2003. The cluster environments and gaseous halos of distant radio galaxies. Ph. D. thesis, Leiden University, P.O. Box 9504, 2300 RA Leiden, The Netherlands
- Kurk, J. D., Pentericci, L., Overzier, R. A., Röttgering, H. J. A., & Miley, G. K. 2004a, A&A, 428, 817
- Kurk, J. D., Pentericci, L., Röttgering, H. J. A., & Miley, G. K. 2004b, A&A, 428, 793
- Mancini, C., et al. 2010, 401, 933
- Maraston, C. 2005, MNRAS, 362, 799
- Miley, G. K., et al. 2006, ApJ, 650, L29
- Mosleh, M., Williams, R. J., Franx, M., & Kriek, M. 2011, ApJ, 727, 5
- Naab, T., Johansson, P. H., & Ostriker, J. P. 2009, ApJ, 699, 178
- Nordon, R., et al. 2010, A&A, 518, L24
- Oke, J. B. 1974, ApJS, 27, 21
- Oser, L., Ostriker, J. P., Naab, T., Johansson, P. H., & Burkert, A. 2010, ApJ, 725, 2312
- Peng, C. Y., Ho, L. C., Impey, C. D., & Rix, H.-W. 2002a, AJ, 124, 266
- Peng, E. W., Ford, H. C., Freeman, K. C., & White, R. L. 2002b, AJ, 124, 3144
- Pentericci, L., Kurk, J. D., Carilli, C. L., Harris, D. E., Miley, G. K., & Röttgering, H. J. A. 2002, A&A, 396, 109
- Salimbeni, S., Fontana, A., Giallongo, E., Grazian, A., Menci, N., Pentericci, L., & Santini, P. 2009, in American Institute of Physics Conference Series, ed. G. Giobbi, A. Tornambe, G. Raimondo, M. Limongi, L. A. Antonelli, N. Menci, & E. Brocato, Volume 1111 of American Institute of Physics Conference Series 207
- Saracco, P., Longhetti, M., & Andreon, S. 2009, 392, 718
- Sérsic, J. L. 1968, Atlas de galaxias australes Cordoba, Argentina: Observatorio Astronomico, 1968
- Steidel, C. C., Adelberger, K. L., Shapley, A. E., Erb, D. K., Reddy, N. A., & Pettini, M. 2005, ApJ, 626, 44
- Stevens, J. A., et al. 2003, Nature, 425, 264
- Tanaka, M., De Breuck, C., Venemans, B., & Kurk, J. 2010, A&A, 518, A18
- Toft, S., Franx, M., van Dokkum, P., Förster Schreiber, N. M., Labbe, I., Wuyts, S., & Marchesini, D. 2009, ApJ, 705, 255
- Toft, S., et al. 2007, ApJ, 671, 285
- van der Wel, A., Bell, E. F., van den Bosch, F. C., Gallazzi, A., & Rix, H.-W. 2009, ApJ, 698, 1232
- van der Wel, A., et al. 2011, ApJ, 730, 38
- van Dokkum, P. G. 2005, AJ, 130, 2647
- Dokkum, van Pieter G., et al. 2008, 677, 5
- Williams, R. J., Quadri, R. F., Franx, M., van Dokkum, P., Toft, S., Kriek, M., & Labbé, I. 2010, ApJ, 713, 738
- Wuyts, S., Labbé, I., Schreiber, N. M. F., Franx, M., Rudnick, G., Brammer, G. B., & van Dokkum, P. G. 2008, ApJ, 682, 985
- Zirm, A. W., et al. 2008, ApJ, 680, 224
- Zirm, A. W., et al. 2007, ApJ, 656, 66

Table 1
Protocluster Candidates

Object Object	Photometric Redshift	Odds	H_{160} (AB)	Line	Stellar Mass ($\log(M_{\odot})$)	Specific SFR ($\log(\text{yr}^{-1})$)	Effective Radius ($''$)	Effective Radius (kpc)	Mass Density ($10^9 M_{\odot} \text{kpc}^{-2}$)
Quiescent Protocluster Galaxies									
312	2.24	1.00	21.98 ± 0.01	0	$11.33^{+0.04}_{-0.04}$	-99.00	0.23 ± 0.09	1.89	9.67 ± 6.5
394	2.23	1.00	24.07 ± 0.01	0	$10.65^{+0.20}_{-0.20}$	-11.24	0.14 ± 0.07	1.20	4.98 ± 2.6
399	2.49	0.98	24.20 ± 0.01	0	$10.59^{+0.20}_{-0.16}$	-11.24	0.23 ± 0.09	1.91	1.78 ± 0.4
493	2.12	1.00	22.73 ± 0.01	0	$11.13^{+0.03}_{-0.04}$	-99.00	0.19 ± 0.07	1.58	8.56 ± 6.2
507	2.16	1.00	22.48 ± 0.01	0	$11.04^{+0.05}_{-0.03}$	-99.00	0.06 ± 0.06	0.47	80.14 ± 52.9
547	2.10	1.00	22.68 ± 0.01	0	$10.97^{+0.08}_{-0.03}$	-11.72	0.09 ± 0.08	0.78	24.21 ± 14.2
574	2.13	1.00	23.33 ± 0.01	0	$10.65^{+0.04}_{-0.04}$	-99.00	0.14 ± 0.09	1.17	5.15 ± 3.6
599	2.54	1.00	23.89 ± 0.01	0	$10.75^{+0.21}_{-0.05}$	-12.20	0.15 ± 0.08	1.22	6.41 ± 1.0
Star-forming Protocluster Galaxies									
347	2.08	0.92	23.69 ± 0.01	0	9.69	-8.79	0.19 ± 0.05	1.57	0.31
456	2.06	0.95	23.57 ± 0.07	0	10.49	-9.27	0.63 ± 0.06	5.19	0.18
595	2.06	0.91	23.47 ± 0.01	0	10.24	-8.79	0.21 ± 0.07	1.72	0.92
Line-emitting Candidates ^a									
700	2.16	...	24.02 ± 0.02	1	0.23 ± 0.06	1.88	...
463	2.16	...	24.51 ± 0.03	1
1078	2.16	...	22.94 ± 0.01	1	0.17 ± 0.06	1.38	...
1070	2.16	...	23.44 ± 0.02	1
511	2.16	...	24.50 ± 0.01	1
516	2.16	...	24.07 ± 0.01	1	0.14 ± 0.08	1.15	...
575	2.16	...	24.62 ± 0.02	1	0.01 ± 0.03	0.09	...
988	2.16	...	23.41 ± 0.01	1	0.32 ± 0.06	2.67	...
536	2.16	...	23.90 ± 0.01	1	0.13 ± 0.08	1.11	...
1069	2.16	...	23.91 ± 0.01	1	0.00 ± 0.54	0.01	...
457	2.16	...	23.84 ± 0.01	1
451	2.16	...	23.74 ± 0.01	1
275	2.16	...	23.62 ± 0.01	1	0.12 ± 0.06	0.96	...
897	2.16	...	24.09 ± 0.01	1	0.11 ± 0.05	0.92	...
300	2.16	...	22.50 ± 0.01	1
311	2.16	...	23.94 ± 0.01	1	6.77 ± 4.36	56.15	...
361	2.16	...	24.50 ± 0.01	1	0.03 ± 0.04	0.27	...
365	2.16	...	26.16 ± 0.06	1
215	2.16	...	24.09 ± 0.01	1	0.14 ± 0.08	1.18	...
448	2.16	...	21.93 ± 0.02	1
435	2.16	...	23.74 ± 0.01	1
431	2.16	...	22.61 ± 0.01	1
Confirmed Line-emitting Galaxies									
53	2.16	...	24.00 ± 0.01	2	0.02 ± 0.04	0.19	...
263	2.16	...	24.01 ± 0.01	2	0.18 ± 0.08	1.52	...
270	2.16	...	21.11 ± 0.01	2
450	2.16	...	22.75 ± 0.01	2
945	2.16	...	23.79 ± 0.01	2	0.03 ± 0.02	0.22	...
289	2.16	...	22.05 ± 0.01	2	11.52	-11.24	0.43 ± 0.09	3.53	4.22
757	2.16	2	10.54	-9.27
561	2.16	...	21.99 ± 0.01	2	11.23	-12.20	0.86 ± 0.09	7.09	0.54
296	2.16	...	22.27 ± 0.01	2	10.50	-8.18	0.10 ± 0.07	0.84	7.10
648	2.16	...	23.38 ± 0.01	2	0.14 ± 0.06	1.18	...
535	2.16	...	23.90 ± 0.01	2	0.14 ± 0.05	1.19	...
387	2.16	...	24.70 ± 0.02	2	0.06 ± 0.04	0.47	...

^a Narrow-band selected objects that are not yet spectroscopically confirmed.

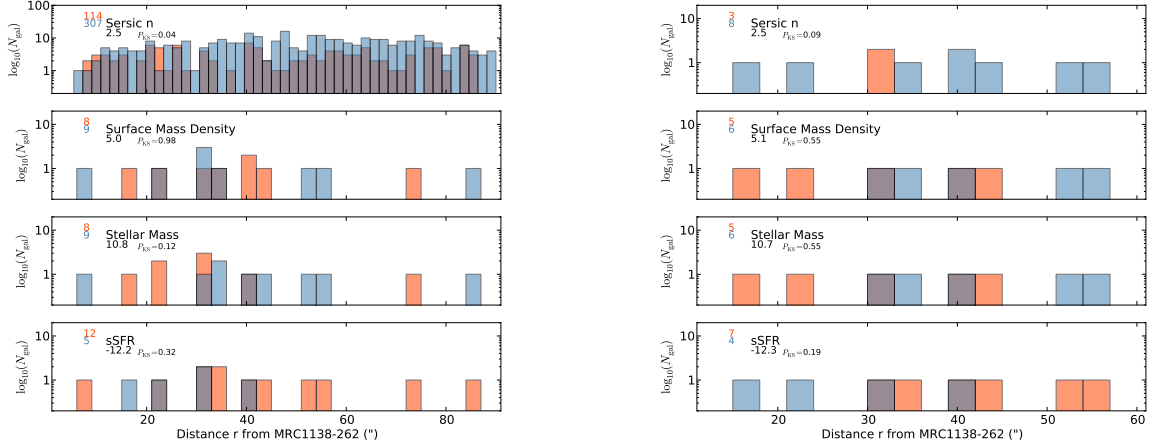


Figure 7. Radial (measured from the radio galaxy) distributions of galaxies as a function of four derived physical parameters. Top to bottom: Sérsic n value, surface mass density (Σ), stellar mass (M_*) and specific star-formation rate. For each parameter we have made a single cut of the total sample into two bins and plotted those two histograms separately for those above (orange) and below (blue) this cut. The value of the cut is shown below the parameter name and the number of galaxies in each bin to the left of the name. Finally, the KS probability, that the two histograms are drawn from the same parent distribution is also shown.